

## Cardiovascular consequences of $K_{ATP}$ overactivity in Cantu syndrome

Yan Huang, ... , Maria S. Remedi, Colin G. Nichols

*JCI Insight*. 2018;3(15):e121153. <https://doi.org/10.1172/jci.insight.121153>.

Research Article

Cardiology

Cantu syndrome (CS) is characterized by multiple vascular and cardiac abnormalities including vascular dilation and tortuosity, systemic hypotension, and cardiomegaly. The disorder is caused by gain-of-function (GOF) mutations in genes encoding pore-forming (Kir6.1, *KCNJ8*) and accessory (SUR2, *ABCC9*) ATP-sensitive potassium ( $K_{ATP}$ ) channel subunits. However, there is little understanding of the link between molecular dysfunction and the complex pathophysiology observed, and there is no known treatment, in large part due to the lack of appropriate preclinical disease models in which to test therapies. Notably, expression of Kir6.1 and SUR2 does not fully overlap, and the relative contribution of  $K_{ATP}$  GOF in various cardiovascular tissues remains to be elucidated. To investigate pathophysiologic mechanisms in CS we have used CRISPR/Cas9 engineering to introduce CS-associated SUR2[A478V] and Kir6.1[V65M] mutations to the equivalent endogenous loci in mice. Mirroring human CS, both of these animals exhibit low systemic blood pressure and dilated, compliant blood vessels, as well dramatic cardiac enlargement, the effects being more severe in V65M animals than in A478V animals. In both animals, whole-cell patch-clamp recordings reveal enhanced basal  $K_{ATP}$  conductance in vascular smooth muscle, explaining vasodilation and lower blood pressure, and demonstrating a cardinal role for smooth muscle  $K_{ATP}$  dysfunction in CS etiology. Echocardiography confirms in situ cardiac enlargement and increased cardiac output in both animals. Patch-clamp recordings reveal reduced ATP sensitivity of [...]

Find the latest version:

<https://jci.me/121153/pdf>



# Cardiovascular consequences of $K_{ATP}$ overactivity in Cantu syndrome

Yan Huang,<sup>1,2</sup> Conor McClenaghan,<sup>1,2</sup> Theresa M. Harter,<sup>1,2</sup> Kristina Hinman,<sup>2</sup> Carmen M. Halabi,<sup>3</sup> Scot J. Matkovich,<sup>4</sup> Haixia Zhang,<sup>1,2</sup> G. Schuyler Brown,<sup>1,2</sup> Robert P. Mecham,<sup>2</sup> Sarah K. England,<sup>1,4</sup> Attila Kovacs,<sup>5</sup> Maria S. Remedi,<sup>1,5</sup> and Colin G. Nichols<sup>1,2</sup>

<sup>1</sup>Center for the Investigation of Membrane Excitability Diseases, and Departments of <sup>2</sup>Cell Biology and Physiology,

<sup>3</sup>Pediatrics, <sup>4</sup>Obstetrics and Gynecology, and <sup>5</sup>Medicine, Washington University School of Medicine, St. Louis, Missouri, USA.

Cantu syndrome (CS) is characterized by multiple vascular and cardiac abnormalities including vascular dilation and tortuosity, systemic hypotension, and cardiomegaly. The disorder is caused by gain-of-function (GOF) mutations in genes encoding pore-forming (Kir6.1, *KCNJ8*) and accessory (*SUR2*, *ABCC9*) ATP-sensitive potassium ( $K_{ATP}$ ) channel subunits. However, there is little understanding of the link between molecular dysfunction and the complex pathophysiology observed, and there is no known treatment, in large part due to the lack of appropriate preclinical disease models in which to test therapies. Notably, expression of Kir6.1 and SUR2 does not fully overlap, and the relative contribution of  $K_{ATP}$  GOF in various cardiovascular tissues remains to be elucidated. To investigate pathophysiologic mechanisms in CS we have used CRISPR/Cas9 engineering to introduce CS-associated SUR2[A478V] and Kir6.1[V65M] mutations to the equivalent endogenous loci in mice. Mirroring human CS, both of these animals exhibit low systemic blood pressure and dilated, compliant blood vessels, as well dramatic cardiac enlargement, the effects being more severe in V65M animals than in A478V animals. In both animals, whole-cell patch-clamp recordings reveal enhanced basal  $K_{ATP}$  conductance in vascular smooth muscle, explaining vasodilation and lower blood pressure, and demonstrating a cardinal role for smooth muscle  $K_{ATP}$  dysfunction in CS etiology. Echocardiography confirms in situ cardiac enlargement and increased cardiac output in both animals. Patch-clamp recordings reveal reduced ATP sensitivity of ventricular myocyte  $K_{ATP}$  channels in A478V, but normal ATP sensitivity in V65M, suggesting that cardiac remodeling occurs secondary to  $K_{ATP}$  overactivity outside of the heart. These SUR2[A478V] and Kir6.1[V65M] animals thus reiterate the key cardiovascular features seen in human CS. They establish the molecular basis of the pathophysiological consequences of reduced smooth muscle excitability resulting from SUR2/Kir6.1-dependent  $K_{ATP}$  GOF, and provide a validated animal model in which to examine potential therapeutic approaches to treating CS.

## Introduction

Cantu syndrome (CS) was first recognized as a distinct pathology 35 years ago (1). The syndrome is extremely complex, with patients typically demonstrating a host of cardiovascular features including marked cardiomegaly, vascular dilation and tortuosity, low blood pressure, persistence of fetal circulation, and pulmonary hypertension (2–6), in addition to hypertrichosis and acromegaloid facial features (7, 8). The molecular basis is now clear: CS results from mutations in the *ABCC9* and *KCNJ8* genes, which encode the regulatory ABCC9 (SUR2) sulfonylurea receptor and pore-forming KCNJ8 (Kir6.1) subunits, respectively, of ATP-sensitive potassium ( $K_{ATP}$ ) channels (9–12). Expressed in various tissues in the body,  $K_{ATP}$  channels are nucleotide-gated, potassium-selective channels that couple cellular metabolism to electrical excitability. *KCNJ8* and *ABCC9* are adjacent genes on human chromosome 12p12.1, and there is a paralogous pair of genes (*KCNJ11* [Kir6.2] and *ABCC8* [SUR1]) on chromosome 11p15.1, with the consequence that multiple subunit combinations may be present in  $K_{ATP}$  channels in different tissues. Heterogeneity is further increased by the existence of variably spliced SUR isoforms; particularly prominent are 2 major splice isoforms of SUR2: SUR2A and SUR2B (13–15).  $K_{ATP}$  channels in vascular smooth muscle are predominantly formed of Kir6.1 and SUR2B, and regulate vascular tone and blood pressure (16, 17), whereas Kir6.2 and SUR2A predominate in cardiac ventricular myocytes, wherein channel activation can result in

**Authorship note:** YH and CM contributed equally to this work.

**Conflict of interest:** The authors have declared that no conflict of interest exists.

**Submitted:** March 20, 2018

**Accepted:** June 28, 2018

**Published:** August 9, 2018

**Reference information:**

*JCI Insight.* 2018;3(15):e121153.

<https://doi.org/10.1172/jci.insight.121153>.

insight.121153.

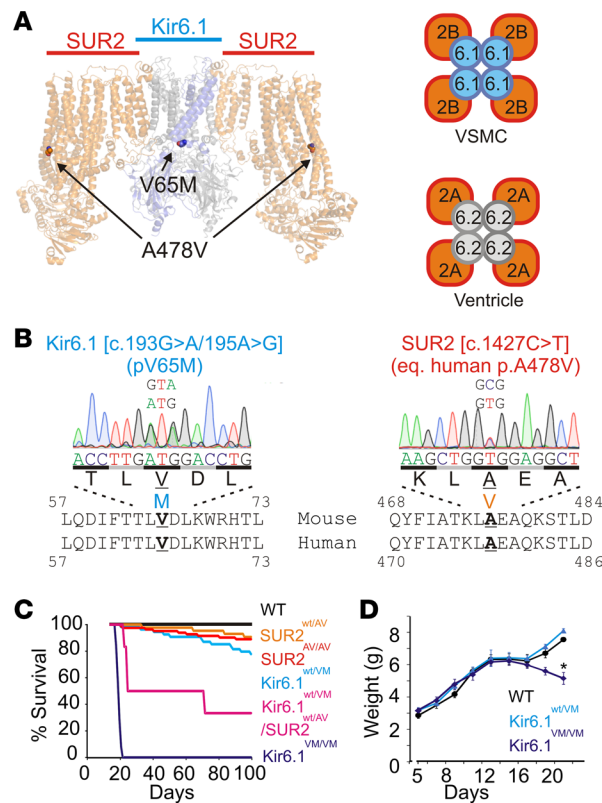


**Figure 1. Generation of the Cantu mice. (A)** Left: Structural representation of the pancreatic Kir6.2/SUR1  $K_{ATP}$  channel (PDB ID: 5WUJ) with the equivalent position of Kir6.1[V65M] and SUR2[A478V] highlighted. Right: Predominant isoform composition of vascular smooth muscle (Kir6.1/SUR2B) and ventricular (Kir6.2/SUR2A)  $K_{ATP}$  channels. **(B)** Sequencing chromatograms from heterozygous Kir6.1<sup>wt/VM</sup> and SUR2<sup>wt/AV</sup> animals. **(C)** Kaplan-Meier survival curves for WT and Cantu animals ( $n = 8-25$  in each genotype). **(D)** Body weight measurements from Kir6.1<sup>wt/VM</sup>, Kir6.1<sup>VM/VM</sup>, and WT littermate mice prior to weaning; Kir6.1<sup>VM/VM</sup> mice lose weight prior to premature death at around 20 days ( $n = 15-25$  animals). Statistical significance was determined by multiway ANOVA followed by  $t$  test pairwise comparison with Bonferroni's correction for multiple comparisons (adjusted  $\alpha = 0.05/3 = 0.017$ ). \* $P < 0.05$ .

significant shortening of the ventricular action potential, which may be cardioprotective in conditions of metabolic or ischemic stress (18, 19).

All identified Kir6.1 and SUR2 CS mutations result in enhanced activity of recombinant  $K_{ATP}$  channels (20–23) and are therefore expected to result in  $K_{ATP}$  GOF in vivo, although this has not been established. Channel GOF is in turn predicted to result in hyperpolarization of the membrane potential and thus a primary decrease of excitability, in all relevant cell types. In smooth muscle, decreased excitability would be predicted to cause vasorelaxation and lowering of blood pressure. In the myocardium, the naive prediction of  $K_{ATP}$  overactivity would be reduced action potential duration, shortening of the QT interval, and reduced contractility as a consequence. How  $K_{ATP}$  overactivity results in the complex and diverse pathophysiology of CS is not trivially obvious and remains largely unexplained. Here, we report the generation of CRISPR/Cas9–modified mice in which CS-associated mutations were introduced into native *KCNJ8* and *ABCC9* loci. These animals establish that both primary and secondary cardiovascular features of CS specifically arise from consequences of GOF missense mutations in Kir6.1 and SUR2, and inform the consequences of vascular smooth muscle inexcitability more generally.

## Results

**Generation of CRISPR/Cas9–modified *KCNJ8*- and *ABCC9*-mutant mice.** CS arises from GOF mutations in *KCNJ8* and *ABCC9*, the genes encoding the  $K_{ATP}$  channel subunits, Kir6.1 and SUR2, respectively. CRISPR/Cas9 gene editing was used to introduce single-nucleotide mutations into the endogenous *KCNJ8* and *ABCC9* gene loci, resulting in protein substitutions that are analogous to Kir6.1[V65M] (V65M in mouse sequence) and SUR2[A478V] (A476V in mouse sequence) in human CS patients (Figure 1, A and B; see Methods).

Founder animals were all viable and fertile, and were bred back to C57BL/6J WT mice to establish several heterozygous lines of each genotype. Homozygous and heterozygous animals from generations F3 onwards were analyzed in all experiments below. There was a minor decrease in survival for heterozygous Kir6.1[V65M] (Kir6.1<sup>wt/VM</sup>), heterozygous SUR2[A478V] mice (SUR2<sup>wt/AV</sup>), and homozygous SUR2[A478V] (SUR2<sup>AV/AV</sup>) mice (Figure 1C). Crossing heterozygous animals from the 2 mutant lines also yielded double-heterozygous Kir6.1<sup>wt/VM</sup>/SUR2<sup>wt/AV</sup> mice, which showed markedly increased mortality (Figure 1C). Survival was drastically decreased in homozygous Kir6.1<sup>VM/VM</sup> mice (Figure 1C), which consistently lost weight prior to dying, within a week or so after weaning (Figure 1D). Autopsy of Kir6.1<sup>VM/VM</sup> mice sacrificed at 3 weeks

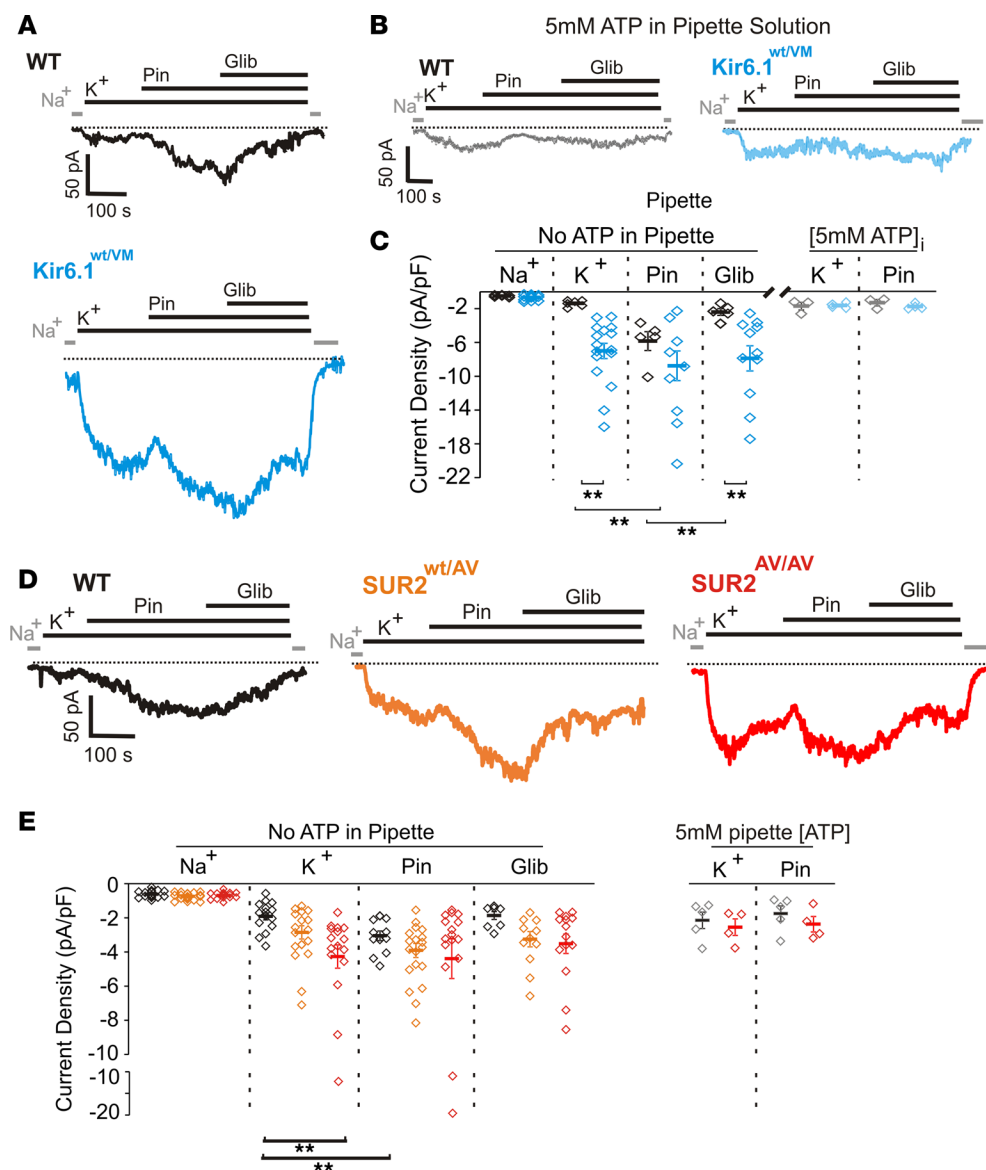


**Figure 2. Smooth muscle  $K_{ATP}$  channels in Kir6.1<sup>wt/vm</sup> and SUR2<sup>wt/av</sup> mice.** (A) Representative whole-cell voltage-clamp recordings from acutely isolated aortic smooth muscle cells from WT (top) and Kir6.1<sup>wt/vm</sup> (bottom) mice. Cells were voltage clamped at  $-70$  mV. (B) Representative whole-cell voltage-clamp recordings from Kir6.1<sup>wt/vm</sup> aortic smooth muscle cells using an intracellular pipette solution containing 5 mM ATP. (C) Summary of whole-cell current densities from voltage-clamp recordings of Kir6.1<sup>wt/vm</sup> aortic smooth muscle cells showing significant increases in basal and pinacidil-activated  $K_{ATP}$  conductances, which are resistant to glibenclamide inhibition ( $n \geq 5$  for WT and 11 for Kir6.1<sup>wt/vm</sup> from  $\geq 3$  mice each). (D) Representative whole-cell voltage-clamp recordings from acutely isolated aortic smooth muscle cells from WT (left, black), heterozygous SUR2<sup>wt/av</sup> (middle, orange), and homozygous SUR2<sup>av/av</sup> (right, red) mice using an intracellular pipette solution absent of nucleotides ( $-70$  mV holding potential). (E) Left: Summary of whole-cell current densities from voltage-clamp recordings of aortic smooth muscle cells from WT, SUR2<sup>wt/av</sup>, and SUR2<sup>av/av</sup> mice showing significant increases in basal and pinacidil-activated  $K_{ATP}$  conductances ( $n \geq 8$  for WT, 11 for SUR2<sup>wt/av</sup>, and 14 for SUR2<sup>av/av</sup> from  $\geq 3$  mice each). Right: Summary of experiments in which 5 mM ATP was included in the patch pipette shown for WT and SUR2<sup>av/av</sup> cells. Statistical significance was determined by multiway ANOVA followed by  $t$  test pairwise comparison with Bonferroni's correction for multiple comparisons. Adjusted  $\alpha = 0.008$  (C) and 0.003 (E). \*\* $P < 0.01$ .

of age revealed distended intestines which, when considered alongside the observed weight loss, may indicate impaired gastrointestinal function.

*Mutation of Kir6.1 and SUR2 results in GOF of native vascular smooth muscle  $K_{ATP}$  channels, but ventricular myocyte  $K_{ATP}$  is only affected in SUR2-mutant mice.* The effects of the introduced mutations on  $K_{ATP}$  channel function were determined using patch-clamp electrophysiology. Firstly, whole-cell patch-clamp recordings, using an intracellular pipette solution containing no ATP (see Methods), revealed a markedly higher ( $\sim 5$ -fold) basal potassium conductance in acutely isolated aortic smooth muscle cells from Kir6.1<sup>wt/vm</sup> mice, compared with WT (Figure 2, A and C). Application of the  $K_{ATP}$  channel opener, pinacidil, provoked significant increase in conductance in WT vascular smooth muscle cells (VSMCs), but this effect was blunted in VSMCs from V65M mice, reflecting basal activation of the mutant  $K_{ATP}$  channels. Subsequent application of the  $K_{ATP}$  channel inhibitor, glibenclamide, markedly reduced the pinacidil-activated conductance in WT VSMCs, but was less effective in V65M (Figure 2, A and C), potentially reflecting the reduced glibenclamide sensitivity of Kir6.1[V65M] channels (21). Importantly, inclusion of a high concentration (5 mM) of ATP in the patch pipette essentially abolished both basal and pinacidil-activated conductances in cells from both WT and V65M VSMCs (Figure 2, B and C), confirming that the observed conductances resulted from  $K_{ATP}$  channel activity.

Because homozygous SUR2<sup>av/av</sup> mice survive to adulthood, we were able to analyze the effect of the SUR2[A478V] mutation in both heterozygous SUR2<sup>wt/av</sup> and homozygous SUR2<sup>av/av</sup> mice. In both

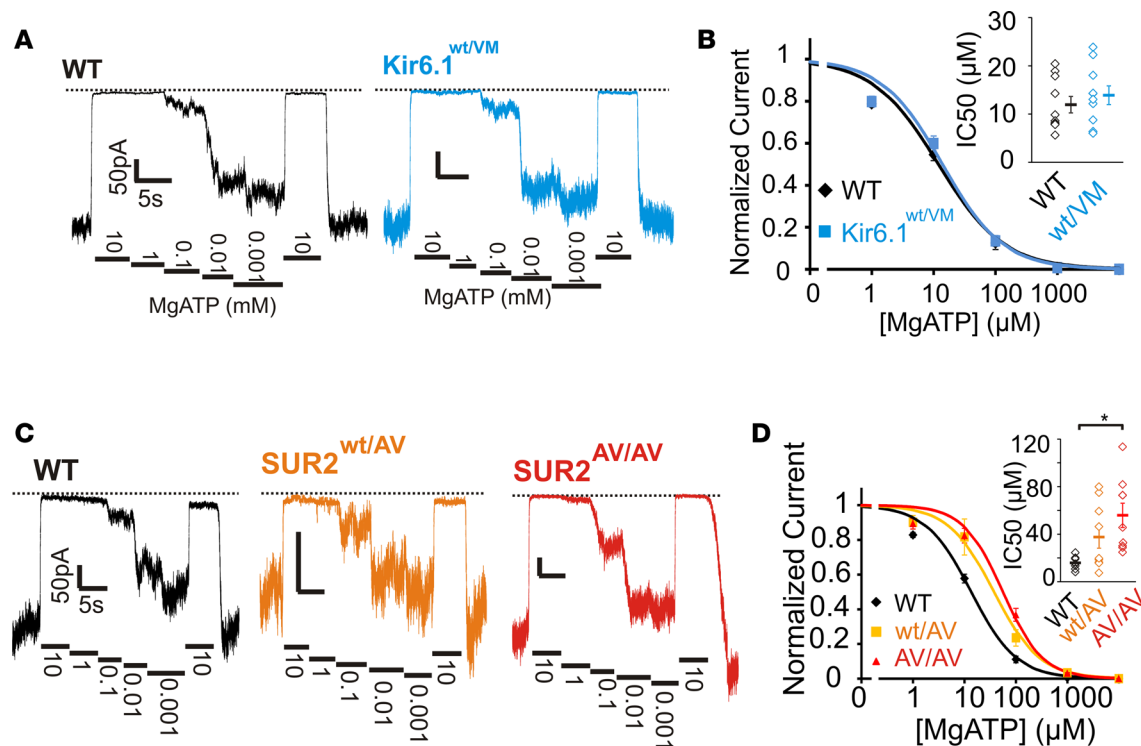


**Figure 3.  $K_{ATP}$  channels in  $Kir6.1^{wt/vm}$  and  $SUR2^{wt/av}$  ventricular myocytes.** (A) Representative inside-out voltage-clamp recordings of  $K_{ATP}$  channel activity from acutely dissociated ventricular myocytes from WT (left) and  $Kir6.1^{wt/vm}$  mice showing the response to MgATP (recording from  $-50$  mV holding potential). (B) Summary [MgATP]-response curves from excised patch experiments ( $IC_{50}$  values from individual experiments shown in inset;  $n = 10$  for WT and  $Kir6.1^{wt/vm}$  from  $\geq 3$  mice each). (C) Representative inside-out voltage-clamp recordings of  $K_{ATP}$  channel activity from acutely dissociated ventricular myocytes from WT (left, black),  $SUR2^{wt/av}$  (middle, orange), and  $SUR2^{av/av}$  (right, red) mice showing the response to MgATP (recording from  $-50$  mV holding potential). (D) Summary MgATP dose-response curves from excised patch experiments shows increased MgATP  $IC_{50}$  in  $SUR2^{wt/av}$  and  $SUR2^{av/av}$  mice ( $IC_{50}$  values from individual experiments shown in inset;  $n = 7$  from WT, 9 from  $SUR2^{wt/av}$ , and  $SUR2^{av/av}$ , from  $\geq 3$  mice each). Statistical significance was determined by multiway ANOVA followed by  $t$  test pairwise comparison with Bonferroni's correction for multiple comparisons (adjusted  $\alpha = 0.017$ ). \* $P < 0.05$ .

cases, basal  $K_{ATP}$  activation was also increased in whole-cell patch-clamp recordings from isolated VSMCs ( $\sim 1.5$ -fold and  $\sim 2.2$ -fold increases for  $SUR2^{wt/av}$  and  $SUR2^{av/av}$ , respectively) (Figure 2, D and E). Glibenclamide reduced currents to near basal levels and, again, inclusion of 5 mM ATP in the pipette solution abolished basal  $K^+$  conductances (Figure 2E), confirming that the increase observed in  $SUR2^{wt/av}$  VSMCs was due to elevated basal  $K_{ATP}$  activity. Notably, the  $K_{ATP}$  GOF in VSMCs from both  $SUR2^{wt/av}$  and  $SUR2^{av/av}$  mice was less than that observed in  $Kir6.1^{wt/vm}$  mice, which is consistent with the effect of these 2 substitutions in recombinantly expressed  $K_{ATP}$  channels (21, 24).

Nucleotide regulation of native  $K_{ATP}$  channels in the heart was assessed using excised, inside-out patch-clamp recordings from acutely dissociated ventricular myocytes. Consistent with the prevailing evidence that ventricular  $K_{ATP}$  channels are composed predominantly of  $Kir6.2/SUR2A$  subunits (i.e., that  $Kir6.1$  is not present in these channels), there was no difference between sensitivity of WT or V65M channel activity to MgATP (Figure 3, A and B), which provides a combined assessment of ATP inhibition and Mg-nucleotide activation of channels. In contrast, excised patch-clamp recordings from  $SUR2^{wt/av}$  and  $SUR2^{av/av}$  ventricular myocytes revealed right-shifted MgATP sensitivity ( $\sim 2$ - and  $\sim 3.5$ -fold increases in  $IC_{50}$ , respectively; Figure 3, C and D), as predicted, given that  $SUR2$  is expressed in ventricular myocytes (15). Thus, in both VSMCs and ventricular myocytes a progressive increase in GOF was observed through heterozygous and homozygous  $SUR2^{wt/av}$  mice. Taken together, these data confirm the expected molecular consequences of the  $Kir6.1[V65M]$  substitution, i.e., that it results in marked GOF of VSMC  $K_{ATP}$ , but has no significant effect on cardiomyocyte  $K_{ATP}$  channels, whereas the  $SUR2[A478V]$  substitution results in GOF of  $K_{ATP}$  channels in both VSMCs and ventricular myocytes.

We subsequently analyzed cellular, organ, and whole-animal phenotypes of the different genotypes. Despite the above qualitatively different outcomes for ventricular  $K_{ATP}$  properties in the  $Kir6.1[V65M]$  and  $SUR2[A478V]$  animals, all of the subsequent features described below were qualitatively similar in

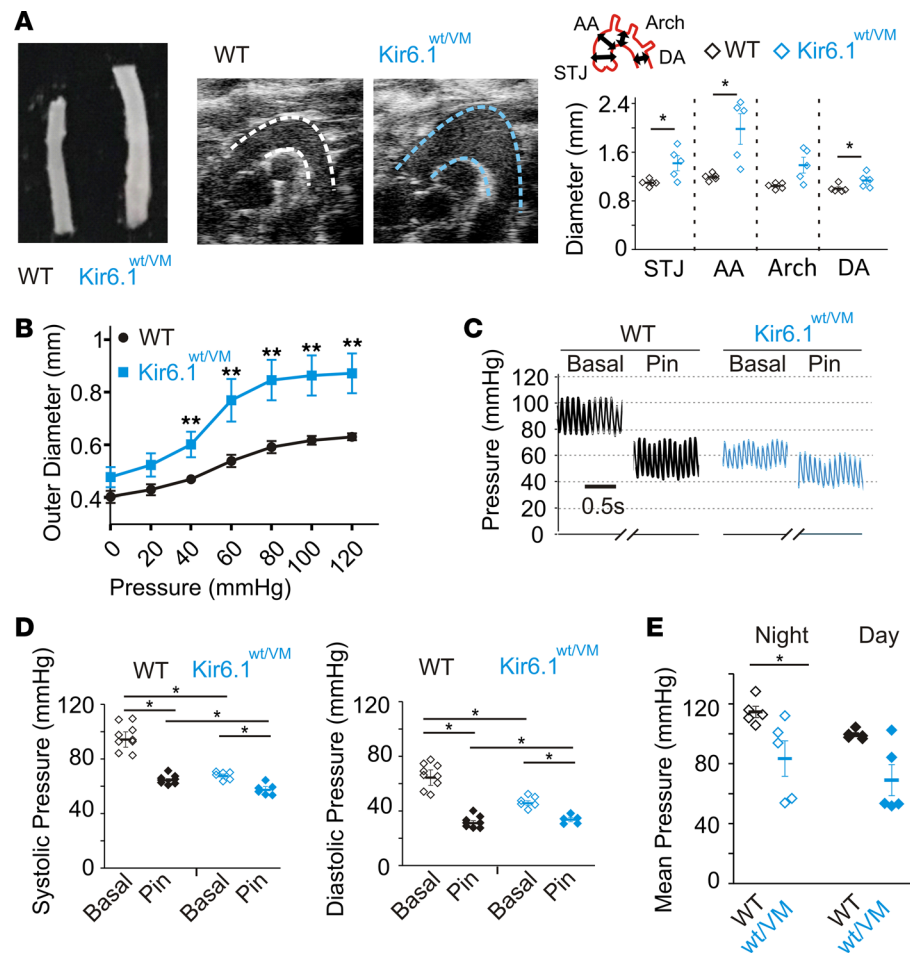


**Figure 4. The effects of  $K_{ATP}$  gain of function on vascular structure and function in  $Kir6.1^{wt/VM}$ .** (A) Left: Isolated descending thoracic aortas show significant gross enlargement in  $Kir6.1^{wt/VM}$  (middle). Sagittal 2D echocardiographic images of the aortic arch reveal significant dilation in  $Kir6.1^{wt/VM}$  mice (aortic boundaries indicated by dashed lines). Right: Measurements of aortic diameter derived from 2D sagittal echocardiographic imaging at different points around the aortic arch in WT (black) and  $Kir6.1^{wt/VM}$  mice (blue). STJ, sinotubular junction; AA, ascending aorta; Arch, aortic arch; DA, descending aorta; as shown in inset;  $n = 5$ ). (B) Vessel compliance measurements from pressurized carotid arteries of WT (black) and  $Kir6.1^{wt/VM}$  (blue) mice ( $n = 4$  for WT,  $n = 7$  for  $Kir6.1^{wt/VM}$ ). (C) Representative blood pressure measurements from anesthetized mice showing decreased basal systemic pressures in  $Kir6.1^{wt/VM}$  mice and blunted response to the  $K_{ATP}$  channel activator pinacidil. (D) Summary data showing systolic (left) and diastolic (right) pressures from anesthetized mice ( $n = 9$  for WT and 6 for  $Kir6.1^{wt/VM}$ ). (E) Telemetric measurements of mean arterial pressure from ambulatory WT and  $Kir6.1^{wt/VM}$  mice ( $n = 5$  for both WT and  $Kir6.1^{wt/VM}$ ). Statistical significance was determined by multi-way ANOVA followed by  $t$  test pairwise comparison with Bonferroni's correction for multiple comparisons. Adjusted  $\alpha = 0.013$  (A), 0.007 (B), 0.013 (D), and 0.025 (E). \* $P < 0.05$ ; \*\* $P < 0.01$ .

both  $Kir6.1[V65M]$  and  $SUR2[A478V]$  animals, but they were more marked in the former. Therefore, we first present in detail the findings from  $Kir6.1[V65M]$  animals, and then present parallel data from the  $SUR2[A478V]$  animals.

**Vascular consequences of  $K_{ATP}$  GOF.** CS patients exhibit dilated and tortuous blood vessels, reduced blood pressure, and decreased pulse wave-velocity (4, 25), suggestive of a chronically relaxed, compliant vasculature. In  $Kir6.1^{wt/VM}$  mice, marked changes in gross vascular structure were observed, including significantly increased aortic diameters (ranging from ~15% to 70% increases around the proximal aorta, not significant at the aortic arch), as measured in vivo by echocardiographic imaging and directly on isolated tissue (Figure 4A). Assessment of pressurized carotid arteries, reflecting noncontractile biomechanical properties of the vessels, revealed significantly increased arterial diameters across the full range of physiological pressures, and increased compliance (Figure 4B).

Marked reduction (~20–25 mmHg) of both systolic and diastolic basal blood pressures were observed in anesthetized 3-month-old  $Kir6.1^{wt/VM}$  mice (Figure 4C). Acute administration of pinacidil, which reduces

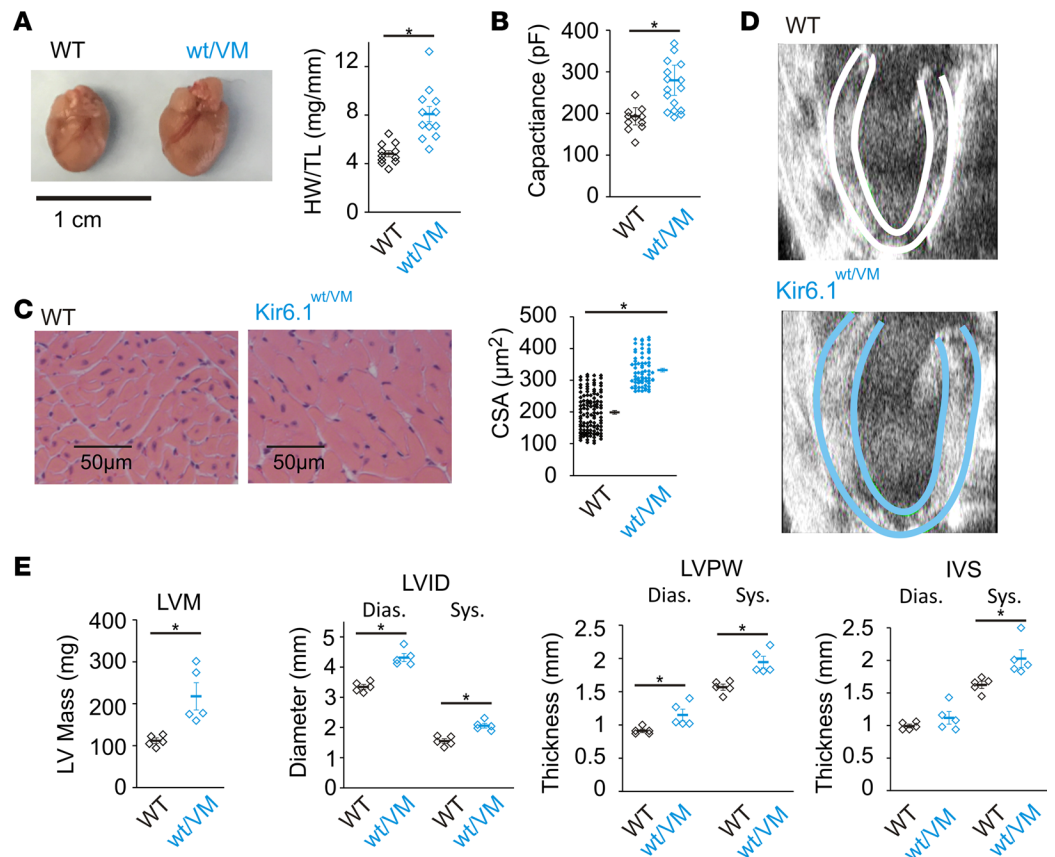


**Figure 5. Cardiac hypertrophy in the Kir6.1<sup>wt/vm</sup> mouse.** (A) Left: Gross heart size is increased in Kir6.1<sup>wt/vm</sup> mice. Right: Heart weight normalized to tibia length (HW/TL; mg/mm;  $n = 11$  for WT and 12 for Kir6.1<sup>wt/vm</sup>). (B) Cardiomegally results from cellular hypertrophy as indicated by increased cell capacitance (measured from whole-cell voltage-clamp recordings of isolated ventricular myocytes ( $n = 11$  for WT and 16 for Kir6.1<sup>wt/vm</sup>)) and (C) from measurements of cell surface area (CSA) from H&E-stained ventricular tissue ( $n = 116$  cells from 3 mice for WT and 69 cells from 3 mice for Kir6.1<sup>wt/vm</sup>). (D) Parasternal long-axis echocardiographic imaging shows increased left ventricle (LV) internal diameter and wall thickness in Kir6.1<sup>wt/vm</sup> (endo- and epicardial boundaries indicated by white or blue lines for WT and Kir6.1<sup>wt/vm</sup>, respectively). (E) M-mode echocardiographic quantification of LV mass (LVM; far left), LV internal diameter (LVID; middle left), LV posterior wall (LVPW; middle right), and intraventricular septum (IVS; far right) are increased in Kir6.1<sup>wt/vm</sup> mice ( $n = 5$  for both). Statistical significance determined by  $t$  test for A, C, and LVM (in E). For LVID, LVPW, and IVS in E, statistical significance was determined by multiway ANOVA followed by  $t$  test pairwise comparison with Bonferroni's correction for multiple comparisons (adjusted  $\alpha = 0.025$ ). \* $P < 0.05$ .

blood pressure by activation of smooth muscle  $K_{ATP}$  in WT mice, was severely blunted in Kir6.1<sup>wt/vm</sup> animals (Figure 4, C and D), reflective of the high basal  $K_{ATP}$  activity and consequently reduced additional activation by pinacidil that is seen in isolated VSMCs (Figure 2). In agreement with data from the anesthetized mice, ambulatory telemetric recordings also showed approximately 30-mmHg decreases in blood pressure in Kir6.1<sup>wt/vm</sup> mice at both night and day, although the difference was not significant during the daytime (Figure 4E).

Therefore, Kir6.1<sup>wt/vm</sup> mice display dilated, compliant arterial vessels resulting in hypotension, mirroring clinical observations in CS patients (4, 25).

**Cardiac hypertrophy in Cantu mice.** Cardiomegaly is a consistent finding in CS patients (25) and is dramatically recapitulated in adult Kir6.1<sup>wt/vm</sup> mice, which show approximately 1.7-fold increases in heart weight (Figure 5A). Estimates of ventricular myocyte size, both from cell capacitance, a correlate of cell membrane surface area, in whole-cell patch clamp recordings of isolated myocytes (Figure 5B), and from H&E-stained ventricular tissue cross sections (Figure 5C), indicate that the increased cardiac mass arises from equivalent cellular hypertrophy.

Echocardiographic imaging *in vivo* also demonstrates an approximately 2-fold increase in left ventricle (LV) mass in Kir6.1<sup>wt/vm</sup> mice, with dilated LV chamber diameters (~30% increase) along with approximately equivalent increases in LV posterior wall and intraventricular septal thickness, compared

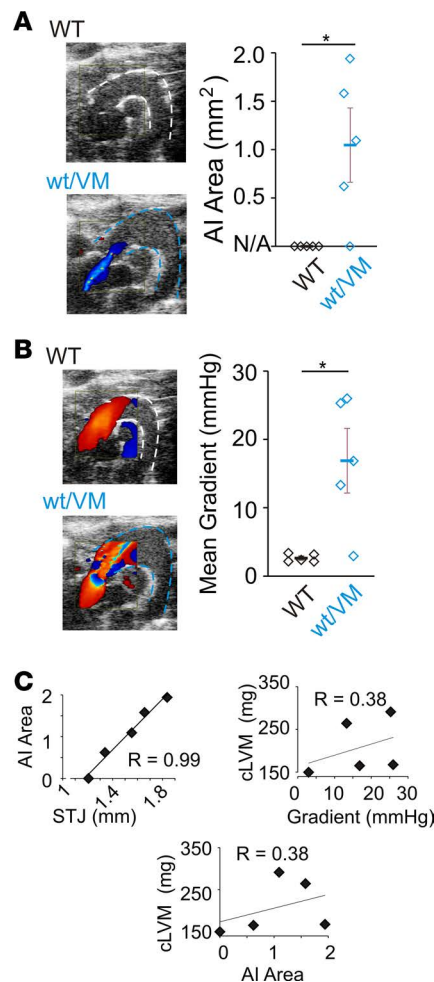


**Figure 6. Aortic insufficiency and aortic regurgitation in the Kir6.1<sup>wt/vm</sup> mouse.** (A) Echocardiographic imaging in diastole reveals aortic valve insufficiency (AI; aortic regurgitation) in 4 of 5 Kir6.1<sup>wt/vm</sup> mice tested (AI not observed in any WT mice;  $n = 5$ ), see also Supplemental Video 1. (B) 2D color Doppler echocardiographic imaging in systole shows aortic valve stenosis in 4 of 5 Kir6.1<sup>wt/vm</sup> but 0 of 5 WT mice (see also Supplemental Video). In A and B, statistical significance was determined by *t* test.  $*P < 0.05$ . (C) Correlation of AI with aortic diameter at the sinotubular junction (STJ) (left); left ventricular mass (LVM; derived from echocardiography) and aortic valve pressure gradient (middle); and LVM and AI area (right) in Kir6.1<sup>wt/vm</sup> mice. R denotes Pearson's correlation coefficient.

with WT (Figure 5, D and E). Consequently, relative wall thickness (RWT) was not significantly different in Kir6.1<sup>wt/vm</sup> mice (RWT for WT  $0.57 \pm 0.02$  mm; for Kir6.1<sup>wt/vm</sup>  $0.52 \pm 0.03$  mm;  $P = 0.1$ ), although suggestive of a mild prevailing eccentric hypertrophy.

Therefore, despite Kir6.1<sup>wt/vm</sup> cardiac myocytes showing essentially normal  $K_{ATP}$  channels, Kir6.1<sup>wt/vm</sup> hearts display chamber dilation and marked cardiac enlargement as a result of cellular hypertrophy, again consistent with echocardiographic findings in CS patients (3, 25).

**Aortic regurgitation and stenosis in Kir6.1<sup>wt/vm</sup> mice.** Cardiac hypertrophy can be associated with valvular defects and/or aortic insufficiency (AI), as has been reported in CS patients (2, 6). Aortic valve function was assessed in vivo by echocardiography. AI and aortic stenosis (AS) of variable extent were observed in color Doppler echocardiographic imaging in 4 of 5 Kir6.1<sup>wt/vm</sup> mice, with 0 of 5 WT littermate controls affected (Figure 6, A and B). The extent of AI was strongly correlated with the measured aortic diameter (sinotubular junction diameter, Figure 6C). In addition, relative AS was apparent in 4 of 5 Kir6.1<sup>wt/vm</sup> mice, in which qualitative valve thickening and restricted leaflet opening were observed (Figure 6, A and B). This was accompanied by elevated mean pressure gradients across the valve in the Kir6.1<sup>wt/vm</sup> mice (Figure 6, A and B, and Supplemental Video 1; supplemental material available online with this article; <https://doi.org/10.1172/jci.insight.121153DS1>).

This combination of AI and increased preload, alongside stenotic or dysfunctional valves with resultant increases in afterload, could contribute to the LV hypertrophy and chamber dilation that are observed. However, there was only a weak correlation between AI or mean gradient and LV mass (Figure 6C), suggesting that both AI and valvular defects may not be primary drivers of hypertrophy in these mice.

**Increased cardiac output in Kir6.1<sup>wt/vm</sup> mice.** In echocardiographic recordings, fractional shortening was not different from WT, but cardiac output was dramatically (~65%) higher, due to equivalently greater stroke volume (Figure 7, A–E). There was a significantly (~80%) higher rate of LV emptying (dV/dT max)

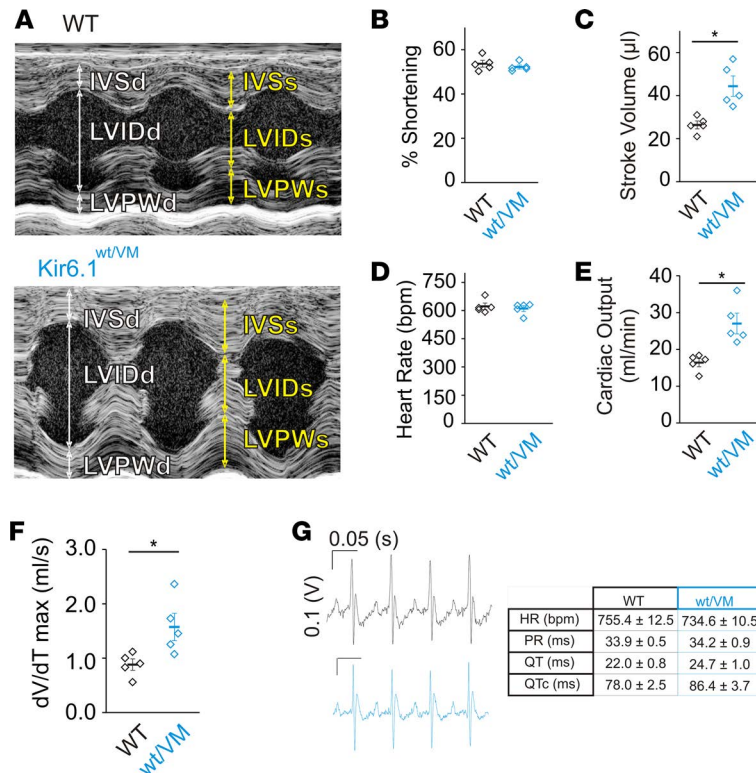


**Figure 7. Cardiac function in WT and Kir6.1<sup>wt/vm</sup> mice.** (A) Representative M-mode echocardiographic imaging of WT (top) and Kir6.1<sup>wt/vm</sup> mice (bottom) showing dilated left ventricle chambers and increased wall diameters. d, diastole; s, systole; IVS, interventricular septum; LVID, left ventricular internal diameter; LVPW, left ventricular posterior wall. (B) Left ventricle (LV) fractional shortening (FS) is unchanged in Kir6.1<sup>wt/vm</sup> as determined from M-mode echocardiograms ( $n = 5$  for both). (C) Stroke volume (SV) is increased in Kir6.1<sup>wt/vm</sup> mice ( $n = 5$  for both). (D) Heart rate (HR) is unchanged in lightly anesthetized Kir6.1<sup>wt/vm</sup> mice during echocardiographic investigation ( $n = 5$  for both genotypes). (E) Cardiac output is markedly increased in Kir6.1<sup>wt/vm</sup> mice due to increased SV and preserved FS. (F) Peak myocardial strain rate (dV/dT max) was increased in Kir6.1<sup>wt/vm</sup> mice as determined from speckle tracking measurements. (G) Left: Representative ECG recordings from awake WT (black) and Kir6.1<sup>wt/vm</sup> (blue) mice. Right: Summary HR, RR-interval, QT duration, and corrected QT (QTc) from WT and Kir6.1<sup>wt/vm</sup> mice (data shown as mean ± SEM;  $n = 7$  for WT,  $n = 11$  for Kir6.1<sup>wt/vm</sup>). Statistical significance determined by *t* test. \* $P < 0.05$ .

in Kir6.1<sup>wt/vm</sup> mice (Figure 7F). This combination of features is consistent with the characteristic high-output cardiac phenotype observed in CS patients (25) that is distinct from typical hypertrophic or dilated cardiomyopathies in which systolic function is impaired. It is consistent with earlier studies of transgenic mice, which showed that expression of  $K_{ATP}$  GOF subunits in either the myocardium or in VSM both result in hypercontractile phenotypes in the heart (25, 26). These outcomes are not directly predicted from any expected electrophysiological consequences of cardiac  $K_{ATP}$  channel GOF. Baseline surface ECG recordings from ambulatory Kir6.1<sup>wt/vm</sup> mice were not markedly different from WT, consistent with patch-clamp studies of isolated ventricular myocytes showing no major changes in Kir6.1<sup>wt/vm</sup> cardiac  $K_{ATP}$  function (Figure 3). Therefore, we suggest that the high-output, enlarged heart observed in Kir6.1<sup>wt/vm</sup> mice may result not from a primary effect on cardiac  $K_{ATP}$  but rather from systemic feedback mechanisms that counter hypotension arising from vascular  $K_{ATP}$  GOF.

*Key CS features are common to both Kir6.1 and SUR2 GOF mutant mice.* Basal systolic and diastolic blood pressures were also decreased relative to WT, in both anesthetized SUR2<sup>AV/AV</sup> and SUR2<sup>wt/AV</sup> mice. Ambulatory blood pressures also decreased in both, but only significantly so in SUR2<sup>AV/AV</sup> mice (Figure 8, A and B). As seen in Kir6.1[V65M] animals, the relative blood pressure-lowering effect of pinacidil was again reduced in SUR2<sup>wt/AV</sup>, and more so in SUR2<sup>AV/AV</sup> (Figure 8, A and C), to the extent that, intriguingly, the lowest pressure achieved with pinacidil was actually higher in SUR2<sup>wt/AV</sup> than WT, and even more so in SUR2<sup>AV/AV</sup> (Figure 8, A and C), the implications of which are considered in the Discussion. As observed in Kir6.1<sup>wt/vm</sup> mice, there were clear trends towards progressively increased vascular

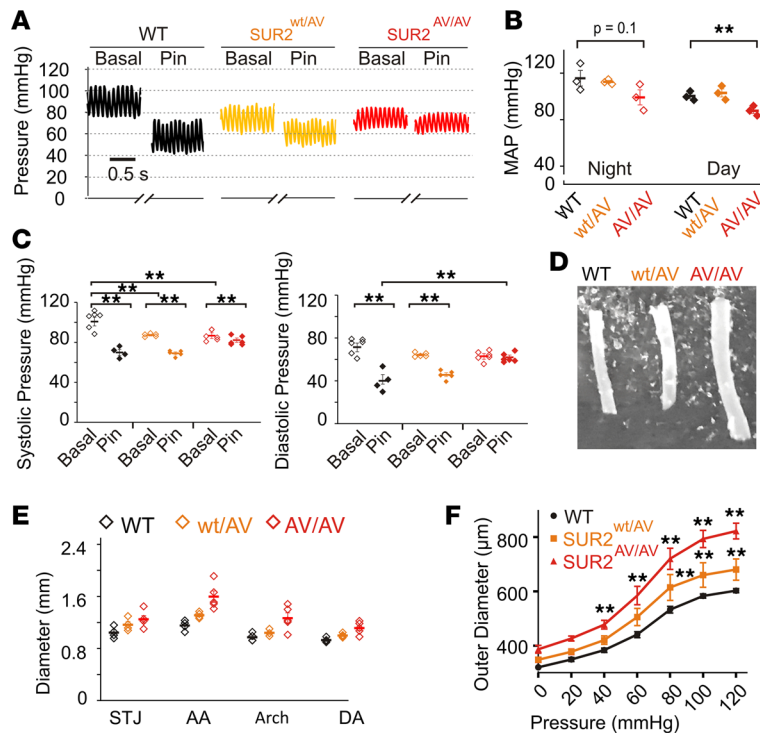


**Figure 8. Vascular consequences in  $SUR2^{wt/AV}$  mice.** (A) Representative blood pressures in anesthetized mice showing decreased basal pressures in  $SUR2^{wt/AV}$  and  $SUR2^{AV/AV}$  mice and blunted response to the  $K_{ATP}$  channel activator pinacidil. (B) Telemetric measurements of mean arterial pressure from ambulatory WT (black),  $SUR2^{wt/AV}$  (orange), and  $SUR2^{AV/AV}$  (red) mice show decreased blood pressure in  $SUR2^{AV/AV}$  mice ( $n = 3$  for each genotype). (C) Summary data showing basal and pinacidil-reduced systolic (left) and diastolic (right) pressures from anesthetized WT,  $SUR2^{wt/AV}$ , and  $SUR2^{AV/AV}$  mice ( $n = 6$  for WT, 5 for  $SUR2^{wt/AV}$ , and 6 for  $SUR2^{AV/AV}$ ). (D) Isolated descending thoracic aortae show progressive dilation in  $SUR2^{wt/AV}$  and  $SUR2^{AV/AV}$  mice. (E) Aortic diameter derived from 2D sagittal echocardiographic imaging at different points around the aortic arch in WT (black),  $SUR2^{wt/AV}$  (orange), and  $SUR2^{AV/AV}$  (red). STJ, sinotubular junction; AA, ascending aorta; Arch, aortic arch; DA, descending aorta; as shown in inset;  $n = 3$  each). (F) Vessel compliance in pressurized carotid arteries of WT (black),  $SUR2^{wt/AV}$  (orange), and  $SUR2^{AV/AV}$  (red) mice reveal increased diameters in mutant mice across full pressure range ( $n = 4$  for WT, 5 for  $SUR2^{wt/AV}$ , and 5 for  $SUR2^{AV/AV}$ ). Statistical significance was determined by multiway ANOVA followed by  $t$  test pairwise comparison with Bonferroni's correction for multiple comparisons. Adjusted  $\alpha = 0.008$  (B), 0.006 (C), and 0.004 (F). \*\* $P < 0.01$ .

diameters, both in vivo in echocardiographic imaging and ex vivo in pressurized compliance measurements on isolated vessels, for  $SUR2^{wt/AV}$  and  $SUR2^{AV/AV}$  mice (Figure 8, D–F).

Marked cardiomegaly was also observed in both  $SUR2^{wt/AV}$  and  $SUR2^{AV/AV}$  mice (~1.2- and ~1.6-fold increases, respectively; Figure 9A), which cell surface area measurements again revealed to result from cellular hypertrophy (Figure 9B). Again, echocardiographic measurements revealed maintained fractional shortening, despite LV dilation, while cardiac output and stroke volume were significantly increased (Figure 9, C–E). Reflecting the generally weaker phenotype in the  $SUR2$ -mutant mice, AI was not observed in any of 5  $SUR2^{wt/AV}$  mice, but was observed in 1 of 5  $SUR2^{AV/AV}$  mice, while no littermate controls were affected (data not shown).

## Discussion

*The pathophysiological effects of  $K_{ATP}$  GOF in CS.* Autosomal dominant GOF mutations in *KCNJ8* and *ABCC9*, the genes encoding the Kir6.1 and SUR2 subunits of  $K_{ATP}$  potassium channels, have now been established as the genetic basis of CS (20–24, 27). In addition to hypertrichosis and coarse facial appearance, CS patients are characterized by a constellation of cardiovascular features, including marked cardiomegaly, vascular dilation and tortuosity, low blood pressure, persistence of fetal circulation, and pulmonary hypertension (2–6). While low blood pressure is a directly predictable primary consequence of vascular  $K_{ATP}$  GOF (Figure 10A), few of the other features, particularly the cardiac enlargement, have a ready explanation, and no direct causal association between the genetic basis and these outcomes has been established.

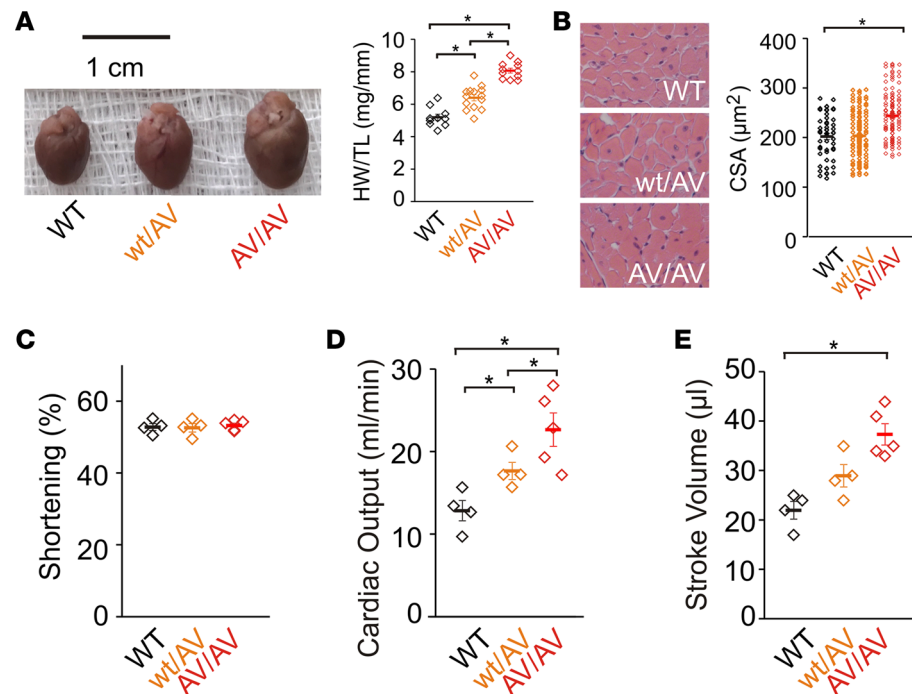


**Figure 9. Cardiac hypertrophy in  $SUR2^{wt/AV}$  mice.** (A) Left: Gross heart size is increased in  $SUR2^{wt/AV}$  and  $SUR2^{AV/AV}$  mice. Right: Heart weight normalized to tibia length (HW/TL; mg/mm;  $n = 10$  for WT, 14 for  $SUR2^{wt/AV}$ , and 14 for  $SUR2^{AV/AV}$ ). (B) Cell surface area (CSA) measurements from H&E-stained ventricular sections shows cellular hypertrophy in  $SUR2^{AV/AV}$  mice ( $n = 45$  cells from 3 mice for WT, 162 cells from 3 mice for  $SUR2^{wt/AV}$ , and 124 cells from 3 mice for  $SUR2^{AV/AV}$ ). (C) Fractional shortening is unchanged in  $SUR2^{wt/AV}$  and  $SUR2^{AV/AV}$  mice as determined from M-mode echocardiographic imaging. (D) Cardiac output is significantly increased in both  $SUR2^{wt/AV}$  and  $SUR2^{AV/AV}$  mice due to increased stroke volume (E) ( $n = 4$  for WT and  $SUR2^{wt/AV}$  and 5 for  $SUR2^{AV/AV}$ ). Statistical significance was determined by multiway ANOVA followed by  $t$  test pairwise comparison with Bonferroni's correction for multiple comparisons (adjusted  $\alpha = 0.017$ ).  $*P < 0.05$ .

In generating animal models in which specific CS mutations are introduced into the equivalent endogenous loci in the mouse genome, we can therefore directly test the causal association. The above studies demonstrate that CS-associated GOF substitutions in both Kir6.1 and SUR2 cause a common constellation of complex cardiovascular features, including increased vascular dilation and compliance, low blood pressure, cardiac hypertrophy, and increased cardiac output. As such, our mouse models recapitulate the key cardiovascular features observed clinically in CS (2, 3, 6). We observe a clear correlation between the extent of basal vascular  $K_{ATP}$  channel activation and the severity of cardiovascular abnormalities through  $SUR2^{wt/AV}$ ,  $SUR2^{AV/AV}$ , and Kir6.1<sup>wt/VM</sup> mice (Figure 10B). Notably, this phenotypic severity also correlates with the previously reported biophysical effects of these mutations (21, 22, 24). In the compound heterozygous Kir6.1<sup>wt/VM</sup>/ $SUR2^{wt/AV}$  and homozygous Kir6.1<sup>VM/VM</sup> animals, the presumably even stronger molecular phenotype results in early death. This precluded detailed assessment of cardiovascular outcomes, but revealed what may be lethal effects of resultant gastrointestinal insufficiency. Interestingly, human CS is likely to represent a more severe clinical categorization within a spectrum of Kir6.1/SUR2 GOF-associated disorders that also includes acromegaloid facial appearance (AFA) syndrome and hypertrichosis with acromegaloid facial features (HAFF) syndrome, in which cardiovascular abnormalities are not reported (28). The severity of human disease may directly correlate with effects on molecular function but some of the same mutations have been reported in both CS and AFA/HAFF patients, so drawing quantitative phenotype-to-genotype comparisons may prove difficult and will require more detailed investigation of multiple mutations (20, 27–29).

*Vascular consequences of  $K_{ATP}$  GOF—primary CS pathological consequences.* That deliberate introduction of these GOF mutations in both *ABCC9* and *KCNJ8* genes converge to the same pathophysiology conclusively demonstrates that the associated pathologies, as observed in CS, result from changes in the  $K_{ATP}$  channel complex that is generated by SUR2 and Kir6.1 protein association (5, 22). It further indicates that the primary consequences must arise in tissue(s) in which both Kir6.1 and SUR2 are expressed. Kir6.1 and SUR2 are clearly both expressed in VSMCs (15, 30), but the situation in cardiac myocytes

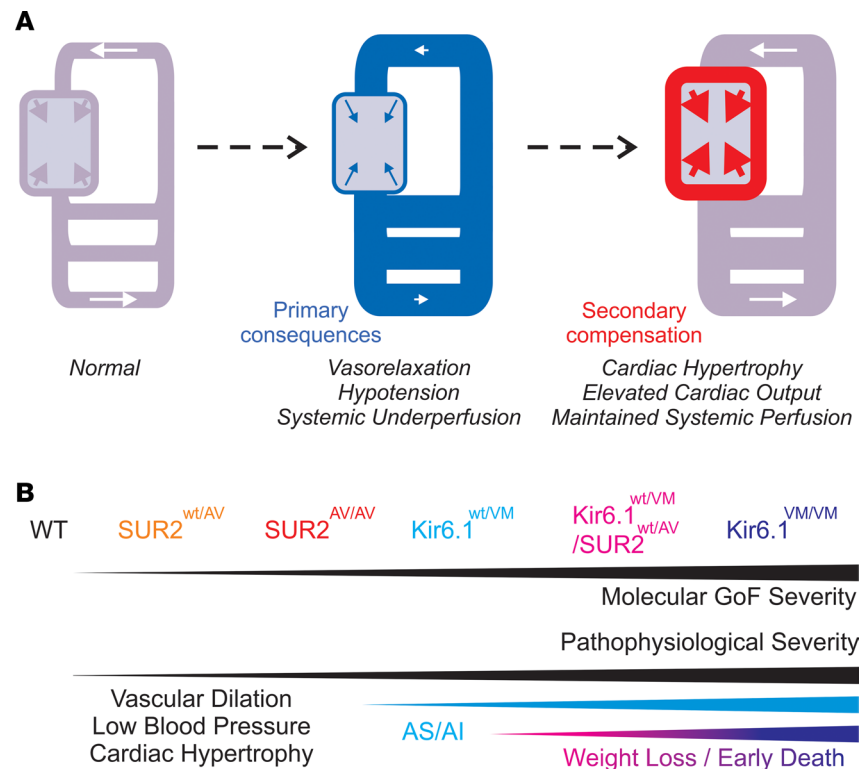


**Figure 10. Progressive cardiovascular consequences of Cantu syndrome.** (A) The primary consequence of  $K_{ATP}$  GOF in the vasculature is reduced excitability, leading to functional and structural vasodilation, low blood pressure, and underperfusion. Secondly, this leads to a compensatory cardiac hypertrophy and hypercontractility. (B) These features are present in even mild (e.g., SUR2<sup>wt/AV</sup>) CS models, but are exacerbated in more severe genotypes (e.g., Kir6.1<sup>wt/VM</sup> and SUR2<sup>AV/AV</sup>). The latter genotypes are associated with premature death, and very early death occurs immediately after weaning in the most severe genotypes (e.g., SUR2<sup>wt/AV</sup>/Kir6.1<sup>wt/VM</sup> and Kir6.1<sup>VM/VM</sup>).

is less clear. Most studies indicate that SUR2 is the primary sulfonylurea receptor in the ventricle, and that Kir6.2 is the pore-forming subunit (31), evidence for Kir6.1 expression being mostly limited to isolated reports of expression in conducting tissue (32). That the most severe CS features are present in Kir6.1[V65M] mutant mice — in which  $K_{ATP}$  GOF is observed in VSMCs but not ventricular myocytes — therefore points to a cardinal role for a non-cardiac muscle origin of the ensuing pathophysiology. Increased  $K_{ATP}$  activity in vascular smooth muscle is predicted to decrease cellular excitability and contractility. Consistent with this, SUR2-selective  $K_{ATP}$  openers acutely decrease vascular tone and lower blood pressure in WT animals (33). Enhanced basal vascular  $K_{ATP}$  activation, as was present in VSMCs from both Kir6.1[V65M] and SUR2[A478V] animals, would thus directly lead to reduced vessel contractility, explaining the lowered blood pressure and reduced response to pinacidil in the whole animal. In SUR2[A478V] animals, the maximum  $K_{ATP}$  overactivity in pinacidil is greater than WT in heterozygous and greatest in homozygous animals, yet the blood pressure in the presence of pinacidil is actually lowest in WT and highest in homozygous animals (Figure 8), counter to naive expectations.

In addition, we see that passive vessel compliance is increased in both genotypes. Increased vessel compliance may reflect increased elastin production in smooth muscle, as has been reported in response to pharmacological activators of  $K_{ATP}$  channels in cultured smooth muscle cells (34), and in the rat aorta (35). It should be noted that endothelial  $K_{ATP}$  channels have also been implicated in blood pressure control (36, 37), and in angiogenesis (38–40). Thus, endothelial dysfunction may also contribute to decreased vascular tone and vessel tortuosity in CS, but this remains to be fully elucidated.

AS, AI, and valvular defects are also reported in association with human CS (2, 6). Here we demonstrate functional defects in the aortic valve of Kir6.1<sup>wt/VM</sup> mice alongside AI and apparent aortic valve stenosis. As extensive dilation is observed throughout the vasculature in CS patients (4), and in the Cantu mice, we hypothesize that AI may be a direct consequence of aortic root dilation. Consistent with this, there is a marked correlation between aortic diameter and AI in Kir6.1<sup>wt/VM</sup> mice. The complex combination of

mutually exacerbating AI and AS would be predicted to increase LV preload and afterload, respectively, and thence to increase cardiac hypertrophy (see below).

*Structural and electrical remodeling in the heart — secondary consequences of  $K_{ATP}$  GOF.* In contrast to the observed vascular manifestations, there are no ready explanations to link  $K_{ATP}$  GOF and the cardiac features of CS. The naive expectation of  $K_{ATP}$  GOF in the heart itself would be action potential shortening, or slowing of the cardiac rate, either or both of which will lead to net reduction in cardiac output. However, in CS patients (25), and in both Kir6.1[V65M] (Figure 5) and SUR2[A478V] (Figure 9) mutant mice, we observe profound cardiac enlargement and enhanced cardiac output. This is despite the different effects of the Kir6.1 and SUR2 mutations on ventricular  $K_{ATP}$  channel properties (Figure 3). Hence we suggest that cardiac enlargement is likely to predominantly arise independently of ventricular  $K_{ATP}$  activity, and to instead be a secondary consequence of vascular dysfunction (Figure 10A). The enlargement observed in the Cantu hearts includes increased LV internal dimensions and wall thickness. This combination is distinct from typical eccentric or concentric hypertrophies arising from volume or pressure overload, respectively, and functionally resembles physiological, exercise-induced, hypertrophy, in which fractional shortening is maintained (41).

*Long-term effects of CS pathophysiology and implications.* The CS combination of cardiac cellular hypertrophy, with chamber and wall enlargement, AI, enhanced cardiac contractility, together with vascular dilation and low blood pressure may represent a unique pathophysiological constellation, distinct from other commonly defined conditions of myocardial hypertrophy. Little is yet known about the progressive nature of CS, but it is notable that the majority of diagnosed patients are children or young adults. Whether this reflects the recent recognition of the condition itself (the genetic basis was only discovered in the last 6 years) and the success of modern palliative therapies, or is an indication of poor long-term prognosis, remains to be elucidated. Cardiac output is elevated in 3-month-old Cantu mice (Figures 5 and 7), but further studies will be required to determine whether the various cardiac abnormalities result in a progressive functional decline with long-term aging, such as is observed in other forms of pathological hypertrophy.

First demonstrated in mice almost 20 years ago (42), recognition of the causal role of GOF mutations in the Kir6.2/SUR1 proteins in neonatal diabetes (43) has led to dramatically improved understanding of the pathophysiological consequences (44), as well as a revolution in therapy using  $K_{ATP}$  channel-blocking sulfonylurea drugs (45, 46). The Cantu mouse models we describe here will provide the opportunity for longitudinal analysis of CS pathophysiology over time, as well as an appropriate preclinical model in which to test the efficacy of  $K_{ATP}$  inhibitors (such as sulfonylureas) or other potential therapies, for what is currently an untreatable syndrome. Moreover, as these mice now confirm a causal link between  $K_{ATP}$  GOF mutations and a host of complex cardiovascular outcomes, they point the way to future studies aimed at understanding the broader consequences of pathophysiological changes in  $K_{ATP}$  channel resulting from nongenetic causes, such as altered cell signaling.

## Methods

### Study approval

Studies were performed in compliance with the standards for the care and use of animal subjects defined in the NIH Guide for the Care and Use of Laboratory Animals (33) and were reviewed and approved by the Washington University Institutional Animal Care and Use Committee.

### CRISPR/Cas9 genome editing

Using CRISPR/Cas9-mediated genome engineering technology (47), we generated knockin mice carrying human GOF mutations in the *ABCC9* or *KCNJ8* genes, which encode the accessory SUR2 and the pore-forming Kir6.1 subunits of the  $K_{ATP}$  channel, respectively. The guide RNA (gRNA) target sequences were predicted using the MIT CRISPR design tool (<http://crispr.mit.edu>). *abcc9* gRNA (5' CATTGCCACGAAGCTGGC-GG 3') or *kcnj8* gRNA (5' ACGCCACTTCAGGTCTACCA 3') were subcloned into BbsI-digested plasmid pX330 (Addgene, 42230). sgRNA activity was validated in vitro by transfection of N2A cells using Roche Xtremegene HP, followed by T7E1 assay (NEB). T7 sgRNA template and T7 Cas9 template were prepared by PCR amplification and gel purification, followed by RNA in vitro transcription with the MEGAshortscript T7 kit (gRNA) or the T7 mMessage mMachine Ultra kit (Cas9). After transcription, RNA was purified with the Megaclear kit (Life Technologies). Single-stranded oligodeoxynucleotide (ssODN) donor DNAs (200 nt) with the appropriate mutation centered within the ODN were synthesized by IDT as ultramer ODNs.

B6CBA F1/J female mice (3–4 weeks old; Jackson Laboratory) were superovulated and mated overnight with B6CBA F1/J male mice (>7 weeks old). Zygotes were harvested from the ampullae of superovulated females and placed in potassium-supplemented simplex optimized medium (KSOM; MR106D) before microinjection. Microinjection of the Cas9, sgRNA, and ssDNA template (at a final concentration of 50 ng/μl Cas9 WT RNA, 25 ng/μl gRNA, and 20 ng/μl ssODN DNA) was performed in flushing holding medium (FHM; MR-024-D; EmbryoMax; Millipore). After injection, zygotes were incubated at 5.5% CO<sub>2</sub> at 37°C for 2 hours, and surviving embryos were transferred to ICR recipient mice by oviduct transfer. Founders were identified using Qiagen pyrosequencer and Pyromark Q96 2.5.7 software. We identified 12 positive founder animals carrying CS mutation mouse SUR2[A476V] (equivalent to human SUR2[A478V]), and 2 positive founder animals carrying the CS mutation Kir6.1[V65M]. All founders were viable and fertile. Successful mutation of founder (F0) mice was verified by Sanger sequencing of genomic DNA and mutant mice were subsequently crossed with C57BL/6J mice to generate heterozygous F1 Kir6.1<sup>wt/vm</sup> and SUR2<sup>wt/av</sup> lines. PCR was used to generate amplicons of *KCNJ8* and *ABCC9* spanning >1 kb on either side of the introduced mutation, from gDNA isolated from mouse tails, and resultant PCR products were sequenced to confirm absence of unintended additional mutations. After verification, one F1 animal from one line of each genotype was selected and further crossed against C57BL/6J to generate F2 heterozygous animals, which were intercrossed to generate F3 heterozygous and heterozygous as well as WT littermates that were used in experiments.

### Patch-clamp electrophysiology

*Isolated VSMCs.* Mice were anesthetized with 2.5% avertin (10 ml/kg, i.p.; Sigma-Aldrich) and the descending aorta was rapidly dissected and placed in ice-cold physiological saline solution (PSS) containing (in mM) 134 NaCl, 6 KCl, 2 CaCl<sub>2</sub>, 1 MgCl<sub>2</sub>, 10 HEPES, and 10 glucose, with pH adjusted to 7.4 with NaOH. Smooth muscle cells were enzymatically dissociated in dissociation solution containing (in mM) 55 NaCl, 80 sodium glutamate, 5.6 KCl, 2 MgCl<sub>2</sub>, 10 HEPES, and 10 glucose, pH 7.3 with NaOH, then placed into dissociation solution containing papain μg/ml 12.5, 1 mg/ml dithioerythritol, and 1 mg/ml BSA for 25 minutes (at 37°C), before transfer to dissociation solution containing 1 mg/ml collagenase (type H/F = 1:2), and 1 mg/ml BSA for 5 minutes (at 37°C). Cells were dispersed by gentle trituration using a Pasteur pipette, plated onto glass coverslips on ice, and allowed to adhere for more than 1 hour before transfer to the recording chamber.

Whole-cell K<sub>ATP</sub> currents were recorded using an Axopatch 200B amplifier and Digidata 1200 (Molecular Devices). Recordings were sampled at 3 kHz and filtered at 1 kHz. Currents were initially measured at a holding potential of –70 mV in a high-Na<sup>+</sup> bath solution containing (in mM) 136 NaCl, 6 KCl, 2 CaCl<sub>2</sub>, 1 MgCl<sub>2</sub>, 10 HEPES, and 10 glucose, with pH adjusted to 7.4 with NaOH before switching to a high-K<sup>+</sup> bath solution (140 KCl, 2 CaCl<sub>2</sub>, 1 MgCl<sub>2</sub>, 10 HEPES, and 10 glucose, with pH adjusted to 7.4 with KOH) in the absence and presence of pinacidil and glibenclamide as indicated. The pipette solution contained (in mM) 110 potassium aspartate, 30 KCl, 10 NaCl, 1 MgCl<sub>2</sub>, 10 HEPES, 0.5 CaCl<sub>2</sub>, 4 K<sub>2</sub>HPO<sub>4</sub>, and 5 EGTA, with pH adjusted to 7.2 with KOH.

*Isolated ventricular myocytes.* Adult mice were anesthetized using 2.5% Avertin (10 ml/kg), and the heart and ascending aorta were removed and immersed in ice-cold calcium-free Wittenberg Isolation Medium (WIM; in mM): 116 NaCl, 5.4 KCl, 8 MgCl<sub>2</sub>, 1 NaH<sub>2</sub>PO<sub>4</sub>, 1.5 KH<sub>2</sub>PO<sub>4</sub>, 4 NaHCO<sub>3</sub>, 12 glucose, 21 HEPES, 2 glutamine plus essential vitamins (GIBCO), and essential amino acids (GIBCO) (pH 7.40). The heart was cannulated via the aorta and Langendorff perfused with WIM for 5 minutes at 37°C, followed by 20-minute perfusion of WIM supplemented with 270 units/ml of collagenase type 2 (Worthington Biochemical) and 10 μM CaCl<sub>2</sub> at 37°C. The heart was then transferred to WIM containing 50 mg/ml BSA, 12.5 mg/ml taurine, and 150 μM CaCl<sub>2</sub>, and ventricular tissue was manually dissociated using forceps before single-cell dissociation by trituration with a fire-polished Pasteur pipette.

Inside-out patch-clamp recordings were made in symmetrical KINT solution that contained (in mM) 140 KCl, 10 HEPES, 1 EGTA (pH 7.4 with KOH). Varying MgATP concentrations were applied using a Dynaflo Resolve perfusion chip (Celletricon). MgCl<sub>2</sub> was added to each solution to achieve a free [Mg<sup>2+</sup>] of 0.5 mM according to calculations using CaBuf (Katholieke Universiteit Leuven). Membrane currents were sampled at 3 kHz, filtered at 1 kHz, at a holding potential of –50 mV using an Axopatch 700B amplifier and Digidata 1200. K<sub>ATP</sub> channel currents in solutions of varying nucleotide concentrations

were normalized to the basal current in the absence of nucleotides and dose-response data were fit with a 4-parameter Hill fit according to the equation: Normalized current =  $I_{min} + (I_{max} - I_{min}) / (1 + ([X] / IC_{50})^H)$ , where the current in  $K_{int} = I_{max} = 1$ ,  $I_{min}$  is the normalized minimum current observed in MgATP,  $[X]$  refers to the concentration of MgATP,  $IC_{50}$  is the concentration of half-maximal inhibition, and  $H$  denotes the Hill coefficient.

### Arterial compliance

After mice were euthanized under isoflurane anesthesia, the left common carotid arteries of 3-week-old mice were excised and placed in PSS containing 130 mM NaCl, 4.7 mM KCl, 1.18 mM  $MgSO_4 \cdot 7H_2O$ , 1.17 mM  $KH_2PO_4$ , 14.8 mM  $NaHCO_3$ , 5.5 mM dextrose, and 0.026 mM EDTA (pH 7.4). The vessels were then cleaned from surrounding fat, mounted on a pressure arteriograph (Danish Myo Technology) and maintained in PSS at 37°C. Vessels were visualized with an inverted microscope connected to a charged-coupled device camera and a computerized system, which allows continuous recording of vessel diameter. Intravascular pressure was increased from 0 to 175 mmHg by 25-mmHg increments and the vessel outer diameter was recorded at each step (12 seconds per step). The average of 3 measurements at each pressure was reported.

### Blood pressure measurement

Mice were anesthetized with 1.5% inhaled isoflurane and restrained on a heating pad to maintain body temperature. A 2- to 3-mm incision was made in the midline of the neck; the thymus and muscle were separated to expose the right carotid artery. A Millar pressure transducer (model SPR-671) was carefully inserted into the right carotid artery and moved to the ascending aorta. Systolic blood pressure, diastolic blood pressure, and heart rate were recorded using the PowerLab data acquisition system (ADInstruments), and data were analyzed using LabChart 7 (ADInstruments). For blood pressure measurements in conscious mice, a radio-telemetry pressure transmitter (Data Science International, DSI) was surgically inserted into the left carotid artery and moved to the ascending aorta, where blood pressures in day and night were recorded by DSI data acquisition system after mice recovered from surgery.

### Heart weight measurement and histology

Mice were anesthetized with 2.5% Avertin and hearts were excised and rinsed with PBS that contained (in mM) 137 NaCl, 2.7 KCl, 10  $Na_2HPO_4$ , and  $KH_2PO_4$  (pH 7.4 with NaOH). The hearts were arrested in diastole with 10% KCl, and blotted to remove excess liquid. Hearts were then weighed and weight was normalized to tibia length. After weighing, the hearts were fixed in 10% buffered formalin for 24 hours, and embedded in paraffin. Sections (3  $\mu$ m) were cut and stained with H&E for the morphometric analysis.

### Echocardiography

Echocardiography was performed using a Vevo 2100 Imaging System (VisualSonics) equipped with a 30-MHz linear-array transducer according to previously published methods (48–50). Cardiac images were obtained by a handheld technique using 100 mg/kg i.p. tribromoethanol anesthetic; aortic images were obtained under 1.5% inhaled isoflurane. M-mode images were used to make LV dimensional measurements. Quantitative image analysis was also performed using a speckle-tracking algorithm to obtain volumetric and strain data. Sagittal 2D images of the aortic arch were used to measure aortic diameters at multiple levels and to obtain Doppler images for pulse wave velocity measurements.

### Statistics

Unless otherwise noted, data were tested for statistical significance using  $t$  test or multiway ANOVA with Bonferroni's correction as applicable, and are presented as mean  $\pm$  SEM. Unless otherwise noted, significance is denoted as  $P < 0.05$ .

### Author contributions

YH, CM, MSR, and CGN conceived the study. YH, CM, TMH, KH, CMH, SJM, HZ, GSB, and AK carried out the experiments. RPM and SKE contributed key technical help. YH, CM, MSR, and CGN wrote the manuscript, which was edited by the other authors.

## Acknowledgments

This work was supported by NIH grant HL140024 (to C.G. Nichols), by Children's Discovery Institute award CH-MI-II-2015-488 (to C.G. Nichols), NIH K08 HL135400 to (C.M. Halabi), and by Pilot and Feasibility Grants, CIMED-17-01 (to M.S. Remedi) and CIMED-18-04 (to C.M. Halabi).

Address correspondence to: Colin G. Nichols, Box 8228, Washington University School of Medicine, 660 S. Euclid Avenue, St. Louis, Missouri 63110, USA. Phone: 314.362.6630; Email: cnichols@wustl.edu.

YH's present address is: Department of Cardiology, Renmin Hospital of Wuhan University, Wuhan, China.

- Cantú JM, García-Cruz D, Sánchez-Corona J, Hernández A, Nazará Z. A distinct osteochondrodysplasia with hypertrichosis-Individualization of a probable autosomal recessive entity. *Hum Genet.* 1982;60(1):36–41.
- Scurr I, et al. Cantú syndrome: report of nine new cases and expansion of the clinical phenotype. *Am J Med Genet A.* 2011;155A(3):508–518.
- Grange DK, Lorch SM, Cole PL, Singh GK. Cantu syndrome in a woman and her two daughters: Further confirmation of autosomal dominant inheritance and review of the cardiac manifestations. *Am J Med Genet A.* 2006;140(15):1673–1680.
- Leon Guerrero CR, et al. Neurologic and neuroimaging manifestations of Cantú syndrome: A case series. *Neurology.* 2016;87(3):270–276.
- Brownstein CA, et al. Mutation of KCNJ8 in a patient with Cantú syndrome with unique vascular abnormalities - support for the role of K(ATP) channels in this condition. *Eur J Med Genet.* 2013;56(12):678–682.
- Nichols CG, Singh GK, Grange DK. KATP channels and cardiovascular disease: suddenly a syndrome. *Circ Res.* 2013;112(7):1059–1072.
- Grange DK, Nichols CG, Singh GK. Cantu syndrome and related disorders. In: Adam MP, Ardinger HH, Pagon RA, Wallace SE, Bean LJH, Stephens K, Amemiya A, eds. *GeneReviews.* Seattle, WA; 2014.
- Nichols CG, Singh GK, Grange DK. KATP channels and cardiovascular disease: suddenly a syndrome. *Circ Res.* 2013;112(7):1059–1072.
- van Bon BW, et al. Cantú syndrome is caused by mutations in ABCC9. *Am J Hum Genet.* 2012;90(6):1094–1101.
- Harakalova M, et al. Dominant missense mutations in ABCC9 cause Cantú syndrome. *Nat Genet.* 2012;44(7):793–796.
- Brownstein CA, et al. Mutation of KCNJ8 in a patient with Cantú syndrome with unique vascular abnormalities - support for the role of K(ATP) channels in this condition. *Eur J Med Genet.* 2013;56(12):678–682.
- Cooper PE, et al. Cantú syndrome resulting from activating mutation in the KCNJ8 gene. *Hum Mutat.* 2014;35(7):809–813.
- Inagaki N, et al. A family of sulfonylurea receptors determines the pharmacological properties of ATP-sensitive K<sup>+</sup> channels. *Neuron.* 1996;16(5):1011–1017.
- Isomoto S, et al. A novel sulfonylurea receptor forms with BIR (Kir6.2) a smooth muscle type ATP-sensitive K<sup>+</sup> channel. *J Biol Chem.* 1996;271(40):24321–24324.
- Chutkow WA, Simon MC, Le Beau MM, Burant CF. Cloning, tissue expression, and chromosomal localization of SUR2, the putative drug-binding subunit of cardiac, skeletal muscle, and vascular KATP channels. *Diabetes.* 1996;45(10):1439–1445.
- Aziz Q, et al. The ATP-sensitive potassium channel subunit, Kir6.1, in vascular smooth muscle plays a major role in blood pressure control. *Hypertension.* 2014;64(3):523–529.
- Li A, et al. Hypotension due to Kir6.1 gain-of-function in vascular smooth muscle. *J Am Heart Assoc.* 2013;2(4):e000365.
- Cole WC, McPherson CD, Sontag D. ATP-regulated K<sup>+</sup> channels protect the myocardium against ischemia/reperfusion damage. *Circ Res.* 1991;69(3):571–581.
- Suzuki M, et al. Role of sarcolemmal K(ATP) channels in cardioprotection against ischemia/reperfusion injury in mice. *J Clin Invest.* 2002;109(4):509–516.
- Harakalova M, et al. Dominant missense mutations in ABCC9 cause Cantú syndrome. *Nat Genet.* 2012;44(7):793–796.
- Cooper PE, McClenaghan C, Chen X, Sary-Weinzinger A, Nichols CG. Conserved functional consequences of disease-associated mutations in the slide helix of Kir6.1 and Kir6.2 subunits of the ATP-sensitive potassium channel. *J Biol Chem.* 2017;292(42):17387–17398.
- Cooper PE, et al. Cantú syndrome resulting from activating mutation in the KCNJ8 gene. *Hum Mutat.* 2014;35(7):809–813.
- McClenaghan C, et al. Cantu syndrome-associated SUR2 (ABCC9) mutations in distinct structural domains result in KATP channel gain-of-function by differential mechanisms. *J Biol Chem.* 2018;293(6):2041–2052.
- Cooper PE, Sala-Rabanal M, Lee SJ, Nichols CG. Differential mechanisms of Cantú syndrome-associated gain of function mutations in the ABCC9 (SUR2) subunit of the KATP channel. *J Gen Physiol.* 2015;146(6):527–540.
- Levin MD, et al. K(ATP) channel gain-of-function leads to increased myocardial L-type Ca(2+) current and contractility in Cantu syndrome. *Proc Natl Acad Sci USA.* 2016;113(24):6773–6778.
- Flagg TP, et al. Remodeling of excitation-contraction coupling in transgenic mice expressing ATP-insensitive sarcolemmal KATP channels. *Am J Physiol Heart Circ Physiol.* 2004;286(4):H1361–H1369.
- van Bon BW, et al. Cantú syndrome is caused by mutations in ABCC9. *Am J Hum Genet.* 2012;90(6):1094–1101.
- Afifi HH, Abdel-Hamid MS, Eid MM, Mostafa IS, Abdel-Salam GM. De novo mutation in ABCC9 causes hypertrichosis acromegaloid facial features disorder. *Pediatr Dermatol.* 2016;33(2):e109–e113.
- Czeschik JC, et al. Wide clinical variability in conditions with coarse facial features and hypertrichosis caused by mutations in ABCC9. *Am J Med Genet A.* 2013;161A(2):295–300.
- Miki T, et al. Mouse model of Prinzmetal angina by disruption of the inward rectifier Kir6.1. *Nat Med.* 2002;8(5):466–472.
- Babenko AP, Gonzalez G, Aguilar-Bryan L, Bryan J. Reconstituted human cardiac KATP channels: functional identity with the

- native channels from the sarcolemma of human ventricular cells. *Circ Res*. 1998;83(11):1132–1143.
32. Bao L, et al. Unique properties of the ATP-sensitive K<sup>+</sup> channel in the mouse ventricular cardiac conduction system. *Circ Arrhythm Electrophysiol*. 2011;4(6):926–935.
33. Jahangir A, Terzic A. K(ATP) channel therapeutics at the bedside. *J Mol Cell Cardiol*. 2005;39(1):99–112.
34. Hayashi A, et al. Minoxidil stimulates elastin expression in aortic smooth muscle cells. *Arch Biochem Biophys*. 1994;315(1):137–141.
35. Raveaud S, et al. Effects of chronic treatment with a low dose of nicorandil on the function of the rat aorta during ageing. *Clin Exp Pharmacol Physiol*. 2009;36(10):988–994.
36. Malester B, et al. Transgenic expression of a dominant negative K(ATP) channel subunit in the mouse endothelium: effects on coronary flow and endothelin-1 secretion. *FASEB J*. 2007;21(9):2162–2172.
37. Aziz Q, Li Y, Anderson N, Ojake L, Tsisanova E, Tinker A. Molecular and functional characterization of the endothelial ATP-sensitive potassium channel. *J Biol Chem*. 2017;292(43):17587–17597.
38. Papapetropoulos A, et al. Hydrogen sulfide is an endogenous stimulator of angiogenesis. *Proc Natl Acad Sci USA*. 2009;106(51):21972–21977.
39. Umaru B, Pyriochou A, Kotsikoris V, Papapetropoulos A, Topouzis S. ATP-sensitive potassium channel activation induces angiogenesis in vitro and in vivo. *J Pharmacol Exp Ther*. 2015;354(1):79–87.
40. Wu Y, et al. Activation of ATP-sensitive potassium channels facilitates the function of human endothelial colony-forming cells via Ca<sup>2+</sup> /Akt/eNOS pathway. *J Cell Mol Med*. 2017;21(3):609–620.
41. Maillat M, van Berlo JH, Molkenin JD. Molecular basis of physiological heart growth: fundamental concepts and new players. *Nat Rev Mol Cell Biol*. 2013;14(1):38–48.
42. Koster JC, Marshall BA, Ensor N, Corbett JA, Nichols CG. Targeted overactivity of beta cell K(ATP) channels induces profound neonatal diabetes. *Cell*. 2000;100(6):645–654.
43. Gloyn AL, et al. Activating mutations in the gene encoding the ATP-sensitive potassium-channel subunit Kir6.2 and permanent neonatal diabetes. *N Engl J Med*. 2004;350(18):1838–1849.
44. Wang Z, York NW, Nichols CG, Remedi MS. Pancreatic  $\beta$  cell dedifferentiation in diabetes and redifferentiation following insulin therapy. *Cell Metab*. 2014;19(5):872–882.
45. Sagen JV, et al. Permanent neonatal diabetes due to mutations in KCNJ11 encoding Kir6.2: patient characteristics and initial response to sulfonylurea therapy. *Diabetes*. 2004;53(10):2713–2718.
46. Wambach JA, Marshall BA, Koster JC, White NH, Nichols CG. Successful sulfonylurea treatment of an insulin-naïve neonate with diabetes mellitus due to a KCNJ11 mutation. *Pediatr Diabetes*. 2010;11(4):286–288.
47. Ran FA, Hsu PD, Wright J, Agarwala V, Scott DA, Zhang F. Genome engineering using the CRISPR-Cas9 system. *Nat Protoc*. 2013;8(11):2281–2308.
48. Cheng SL, et al. Targeted reduction of vascular Msx1 and Msx2 mitigates arteriosclerotic calcification and aortic stiffness in LDLR-deficient mice fed diabetogenic diets. *Diabetes*. 2014;63(12):4326–4337.
49. Schugar RC, Moll AR, André d'Avignon D, Weinheimer CJ, Kovacs A, Crawford PA. Cardiomyocyte-specific deficiency of ketone body metabolism promotes accelerated pathological remodeling. *Mol Metab*. 2014;3(7):754–769.
50. Cheng SL, et al. Vascular smooth muscle LRP6 limits arteriosclerotic calcification in diabetic LDLR<sup>-/-</sup> mice by restraining non-canonical Wnt signals. *Circ Res*. 2015;117(2):142–156.